RESEARCH ARTICLE

National Science Open
5: 20250063, 2026
https://doi.org/10.1360/nso/20250063

Materials Science

Special Topic: Intelligent Materials and Devices

Polypyrrole-modified PVDF-HFP coaxial electrospun composite membranes for intelligent thermal management and electromagnetic interference shielding

Rongjun Wei[1,2,3], Bingqing Quan[1,2,3], Muyi Han[4], Xinpeng Hu[1,2,3,*] & Xiang Lu[1,2,3,*]

[1]*Key Laboratory of Material Chemistry for Energy Conversion and Storage, Huazhong University of Science and Technology, Ministry of Education, Wuhan 430074, China;*
[2]*Hubei Engineering Research Center for Biomaterials and Medical Protective Materials, Huazhong University of Science and Technology, Wuhan 430074, China;*
[3]*Hubei Key Laboratory of Material Chemistry and Service Failure, School of Chemistry and Chemical Engineering, Huazhong University of Science and Technology, Wuhan 430074, China;*
[4]*Department of Materials Science and Engineering, National University of Singapore, Singapore 117575, Singapore*

*Corresponding authors (emails: hxpbest@outlook.com (Xinpeng Hu); luxiang@hust.edu.cn, luxiang_1028@163.com (Xiang Lu))

Received 1 October 2025; Revised 25 November 2025; Accepted 3 December 2025; Published online 4 December 2025

Abstract: The increasing prevalence of extreme environments and the growing severity of electromagnetic pollution make it urgent to develop composites that combine dynamic thermal management with electromagnetic interference (EMI) shielding capabilities. However, it is challenging to integrate all these performances into a single device through a straightforward method. This study reports a novel composite membrane that combines outstanding thermal management capabilities and EMI shielding performance. The fibre membrane, with a distinct core-shell structure, maintains a thermal storage capacity (82.84 J/g) and anti-leakage properties. The *in-situ* polymerised polypyrrole (PPy) endows it with active thermal management capabilities, including Joule heating and solar-to-thermal conversion properties. A satisfactory EMI shielding performance was also achieved, and the shielding effectiveness can be enhanced through a simple origami technique. Moreover, the composite exhibits desirable thermal stability and cycle reliability. In brief, this multifunctional composite film demonstrates significant application potential in wearable textiles for thermal management and EMI shielding.

Keywords: coaxial electrospinning, phase change energy storage, Joule heating, photothermal conversion, electromagnetic interference shielding

INTRODUCTION

The increasing frequency of extreme weather events has posed significant risks to human health and safety, highlighting the urgent need for effective thermal management solutions. Fibers, as fundamental materials for regulating human thermal comfort, have long attracted interest [1–3]. However, pristine fibers lack thermal buffering capacity and cannot maintain stable temperatures under fluctuating conditions, which significantly restricts its practical applications and further development [4,5].

To overcome this limitation, phase change materials (PCMs) have been incorporated into fabrics to regulate temperature by storing and releasing latent heat during phase transitions [6–8]. For example, Xu *et al*. [9] constructed a core-sheath fiber comprising thermoplastic polyurethane (TPU) encapsulating polyethylene glycol (PEG) via a coaxial wet-spinning and photo-crosslinking strategy. This solid-solid phase change fiber achieves a thermal energy storage density of 122.5 J/g, making it suitable for wearable thermal management. In another study, Wang *et al*. [10] fabricated a coaxial electrospun composite fibre with a dodecanol core and a polyacrylate sheath, which exhibits high latent heat (106.9 J/g) and excellent cycling stability. While these approaches improve passive thermal regulation, conventional PCMs suffer from poor flexibility, and fabric-based composites often lack multi-mode thermal management functions to fulfill the varying requirements of practical conditions [11]. Since relying solely on PCMs is often insufficient to meet the demands, incorporating thermal management strategies such as solar-to-thermal and electro-to-thermal conversion capabilities into flexible fabric/PCM systems therefore represents a promising route to enhance thermal comfort and expand their application potential [12,13].

In addition to thermal regulation, effective electromagnetic interference (EMI) shielding performance in textile composites remains an unresolved challenge, particularly due to the growing prevalence of electromagnetic pollution associated with the widespread adoption of 5G communication technologies and the expanding use of portable electronic devices [14]. High-frequency electromagnetic radiation not only causes signal distortion but may also pose serious threats to human health as well as other potential dangers [15,16]. Therefore, mitigating the interference of electromagnetic waves (EMWs) through wearable textiles is of importance for maintaining normal daily routines. The critical dependence of efficient EMI shielding on continuous conductive networks has driven substantial research interest in materials like metals [17], MXenes [18], and carbon-based composites [19,20] in recent years. For instance, a multifunctional and symmetrically structured composite film was fabricated, which exhibits integrated EMI shielding (70.2 dB), efficient thermal management, and robust mechanical properties. This film was constructed with a polypyrrole (PPy) modified aramid nanofibre (ANF) framework, followed by the sequential deposition of tannic acid-treated MXene and silver nanowires (AgNWs) via vacuum-assisted filtration [21]. Similarly, a leather-based composite (LMSN) that simultaneously provides impact resistance, EMI shielding, and thermal management was fabricated by infiltrating MXene into the hierarchical fiber scaffold of leather and subsequently laminating shear-stiffening gel and nonwoven fabric layers, offering a versatile platform for next-generation wearable protective electronics [21]. The high electrical conductivity across these systems facilitates simultaneous multiple internal reflections and efficient absorption, thereby maximizing the attenuation of incident EMWs [22–24]. Although significant achievements, the complicated fabrication process and single-mode thermal management approach render it difficult to meet practical demands. Moreover, MXene exhibits drawbacks such as susceptibility to flaking and environmental oxidation, which can compromise the performance and limit its long-term application in lightweight, foldable, and wearable systems [25,26]. To date, the integration of EMI shielding capability into flexible fabric/PCM composites that also possess solar-to-thermal and electro-to-thermal functions remains a significant challenge.

In this study, we present a multifunctional phase change composite material that combines passive and active thermal regulation with EMI shielding performance (Scheme 1). Our design employs an interfacial engineering strategy in which paraffin wax (PW) serves as the PCM core, encapsulated by poly(vinylidene fluoride-co-hexafluoropropylene) (PVDF-HFP) coaxial electrospun fibers, and further modified with PPy

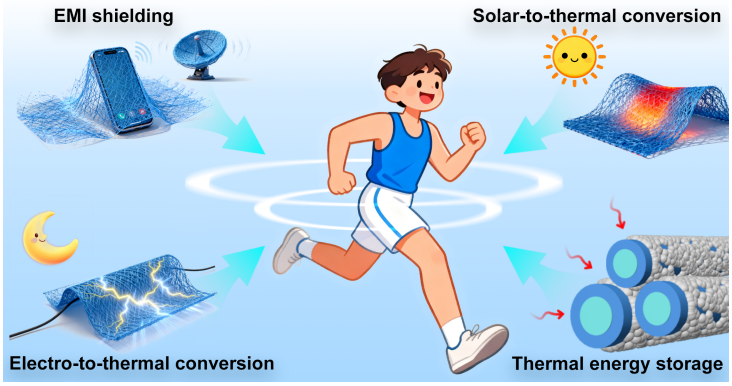

Scheme 1 Schematic illustration of PVDF-PW@PPy composite film based on interfacial engineering strategies for thermal management and EMI shielding.

nanoparticles. PPy is an attractive conductive polymer owing to its intrinsic conductivity and broad spectral absorption [27]. In the proposed composite, PPy imparts efficient electrical conductivity for EMI shielding and Joule heating, as well as excellent solar absorption (~94%) for solar-to-thermal conversion. The resulting PVDF-PW@PPy fiber membrane is lightweight, flexible, and exhibits a favourable thermal storage capacity (82.84 J/g). Moreover, its EMI shielding effectiveness (SE) can be further enhanced through a simple origami-inspired structural design. Overall, this multifunctional composite film demonstrates considerable potential for applications in thermal management and EMI shielding, providing important insights for the development of lightweight, flexible, and sustainable wearable textiles.

RESULTS AND DISCUSSION

In this paper, a phase change composite film with excellent thermal management properties and EMI shielding performance was constructed based on interfacial engineering strategies. We first prepared a PVDF-PW fibre membrane through coaxial electrospinning technology with PW for the core material and PVDF-HFP for the shell material. This fibre membrane combines leakage resistance with phase change energy storage capabilities without compromising flexibility. Subsequently, PPy was polymerised on the surface of PVDF-PW to obtain the PVDF-PW@PPy composite film (Figure 1a). The aggregated PPy exhibits excellent electrical conductivity and light absorption capacity, endowing the composite film with outstanding Joule heating characteristics, photothermal conversion performance, and EMWs resistance capabilities.

The construction effect of PVDF-PW@PPy can be initially assessed through their macro- and micro-structures (Figure 1b). The obtained PVDF-PW membrane is white in colour, with a smooth surface and an average fibre diameter of 2–6 μm. These fibres intertwine with each other and overlap to form a three-dimensional mesh structure. Transmission electron microscopy (TEM) testing shows that PW was encapsulated perfectly inside, forming a distinct ‘core-shell’ structure. This distinct core-shell structure is critical for confining the PW molecular chains during melting, thereby endowing the composite membrane with excellent anti-leakage properties. To verify this, we subject the samples to a 70 °C environment for 2 h.

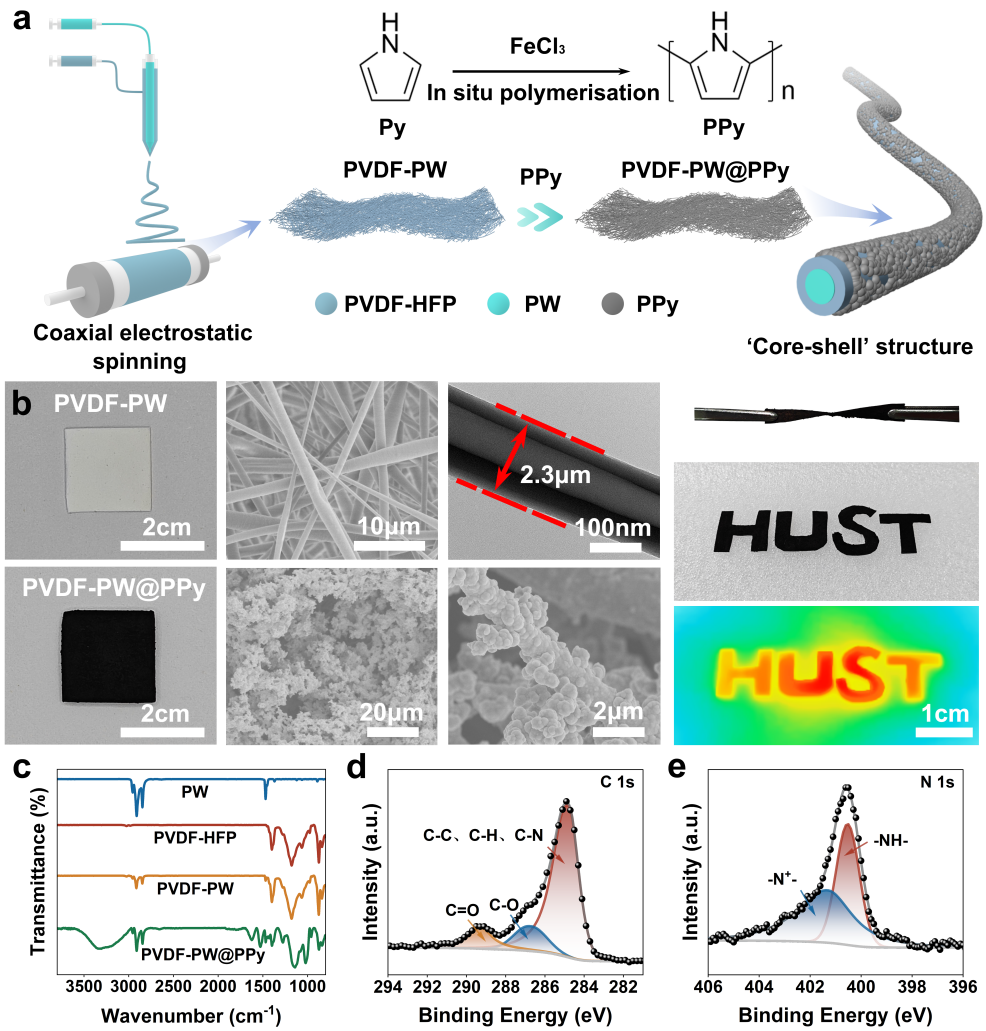

Figure 1 Fabrication process and preparation effect of PVDF-PW@PPy composite film. (a) Preparation process diagram of PVDF-PW@PPy. (b) Macro- and microstructures of the sample. (c) FT-IR curve. (d) High-resolution C 1s curve and (e) N 1s curve of PVDF-PW@PPy.

As shown in Figure S1, while pure PW exhibits severe leakage, both the PVDF-PW and PVDF-PW@PPy composite films retain their structural integrity without any leakage, confirming the effective encapsulation provided by the PVDF-HFP shell. After PPy polymerisation, the PVDF-PW@PPy composite membrane exhibits a more pronounced black appearance. PVDF-PW@PPy composite films prepared with different polymerization times exhibited no discernible color variation (Figure S2). Excellent compatibility was observed between the PPy coating and the PVDF-PW substrate. As can be seen from the scanning electron microscopy (SEM) images that numerous nanoscale PPy particles were uniformly formed on the surface of PVDF-PW. These particles interconnected seamlessly, enveloping the fibrous substrate to constitute a continuous and rough outer layer.

The polymerization time significantly influences the microstructure of PVDF-PW@PPy. Extending the duration of polymerization results in increasingly dense and compact connections among the PPy nanoparticles. At a shorter polymerization time (2 h), PPy only partially covers the PVDF-PW surface, with

discernible gaps present. In contrast, prolonged polymerization (6 h) leads to excessive aggregation of nanoparticles (Figure S3). When the polymerization time was maintained at an intermediate duration of 4 h, a continuous and uniform nanoparticle layer was formed, achieving complete coverage of the PVDF-PW membrane. The prepared PVDF-PW@PPy composite film was approximately 960 μm in thickness. Energy dispersive X-ray spectroscopy (EDS) results indicate that the main characteristic elements C and N of PPy were uniformly distributed on the surface of the fibre membrane after *in situ* polymerisation. Only a small amount of F elements from PVDF-HFP can be observed, which initially demonstrates that the PVDF-PW@PPy composite film was successfully constructed (Figure S4). The obtained PVDF-PW@PPy composite film exhibits excellent flexibility. It could be easily twisted, folded, and bent without causing any damage (Figure S5). The film could also be carefully tailored into 'HUST' patterns, demonstrating outstanding manipulability. The stacked PPy nanoparticles endow the membrane with exceptional photothermal conversion capacity, enabling rapid transformation of solar energy into thermal energy under illumination, as will be illustrated in detail below (Figure 1b).

The successful synthesis of the PVDF-PW@PPy composite membrane can also be demonstrated through a series of chemical characterisation methods, including Fourier transform infrared spectroscopy (FT-IR), X-ray diffraction (XRD) and X-ray photoelectron spectroscopy (XPS) spectra. As shown in Figure 1c, the strong and sharp peaks at 2911 and 2847 cm^{-1} in the FT-IR spectrumare attributed to the asymmetric stretching vibration and symmetric stretching vibration of methylene, respectively, while the peak at 1468 cm^{-1} is attributed to the bending vibration of C–H in PW [28–30]. The characteristic peak of PVDF-HFP at 1400 cm^{-1} belongs to the bending vibration of $–CH_2$. The peak at 1177 cm^{-1} is attributed to the asymmetric stretching vibration of $–CF_2$, while the peak at 872 cm^{-1} corresponds to the symmetric stretching of CF_2 and C–C [31,32]. After PPy polymerisation reaction, the presence of the pyrrole skeleton was confirmed by the appearance of new peaks at 3330 cm^{-1} (N–H stretching vibration), 1536 and 1468 cm^{-1} (C=C stretching vibration), and 1326 cm^{-1} (C–N stretching vibration) [33,34]. In addition, a broad and large characteristic peak appears at around 1145 cm^{-1}, indicating that the polymerised PPy exhibits a conductive state. The above results indicate that Py was polymerised on the PVDF-PW surface under the effect of $FeCl_3$ solution.

In the XRD pattern of PW, several intense diffraction peaks are observed at $2\theta = 7.11°$, 10.60°, 14.07°, and 23.46° [35]. PVDF-HFP exhibits three diffraction peaks at $2\theta = 18.33°$, 19.77°, and 26.68°, corresponding to the (100), (110), and (021) crystal planes of the α-phase, respectively [36]. The presence of polymerized PPy has a negligible influence on the XRD pattern of the composite membrane, which can be attributed to the amorphous nature of PPy (Figure S6). As evidenced by the FT-IR and XRD spectra, all characteristic peaks of PVDF-PW and PPy could be seen in the curves of PVDF-PW@PPy composite and no new peaks were generated, indicating that these two components were combined only through physical methods.

The successful polymerisation of PPy can also be confirmed by XPS analysis (Figure S7). In the high-resolution C 1s spectrum of PVDF-PW@PPy composite film, the obtained spectrum can be fitted into three peaks located at 289.30, 286.80, and 284.80 eV, corresponding to the electronic peaks of C=O, C–O, and C–C/C–H/C–N in the composites (Figure 1d). The $–N^+–$ (401.31 eV) and –NH– (400.52 eV) peaks obtained from the fitted N 1s spectrum correspond to the N elements on the pyrrole units within PPy (Figure 1e) [37,38]. Additionally, PPy significantly influenced the surface properties of the composite film. The water contact angle (WCA) of PVDF-PW was 124° when leaving for 30 s. In contrast, the WCA of the PVDF-

PW@PPy composite film decreased sharply to 36° within just 1 s. The water droplets subsequently spread and absorbed rapidly on the composite surface, indicating that the polymerized PPy effectively transformed the material from hydrophobic to hydrophilic (Figure S8). Hence, it can be inferred from the above results that PPy was successfully polymerised on the surface of PVDF-PW fibres.

The content of PW significantly influences the energy storage performance of the composite film as it acts as the primary PCMs, while the remaining PVDF-HFP and polymerised PPy serve as physical support materials and functional modifiers. Hence, the enthalpy and phase change temperatures of PVDF-PW@PPy composite films with different polymerisation times were tested. It can be seen that pure PW exhibits suitable thermal energy storage capacity and phase change temperatures. The melting and cooling enthalpies (ΔH_m/ΔH_c) were measured to be 229.33 and 232.98 J/g, respectively, while the corresponding phase change temperatures during melting and cooling (T_m/T_c) were 37.72 and 30.52°C, respectively (Figure S9). The values of ΔH_m and ΔH_c for the PVDF-PW fibre membrane decreased to 111.11 and 111.74 J/g, respectively, while the phase change temperatures remained largely unchanged. After PPy polymerisation, the differential scanning calorimetry (DSC) curves of PVDF-PW@PPy composite films under different treatment times were essentially the same (Figure S10). The heat storage capacity of PW was inherited by PVDF-PW@PPy. The values of ΔH_m and ΔH_c were ranged between 86.43–76.50 and 86.78–76.62 J/g, respectively. Both of them decreased with extended polymerisation time (Figure S11), while only the values of T_m and T_c remained relatively stable (Figure S12). Hence, the aggregated PPy has little effect on the melting and cooling processes of the PVDF-PW@PPy composite film, which is beneficial for achieving favourable thermal performance.

The thermal stability of PVDF-PW@PPy composite films was tested (Figure S13). Both pure PW and PVDF-HFP undergo one-step degradation, with maximum degradation temperatures of 227.97 and 461.20 °C, respectively [39,40]. The PVDF-PW membrane prepared by coaxial electrospinning undergoes two processes of degradation, corresponding to the thermal decomposition of PW (200.03 °C) and PVDF-HFP (449.60 °C). The degradation process of PVDF-PW@PPy composite film was changed slightly after PPy treatment, with the maximum degradation temperature rising to 466.18 °C. In addition, the residual carbon rate of PVDF-PW@PPy (27.59%) was slightly higher than that of PVDF-PW (11.63%) within 600 °C. It indicates that the polymerised PPy slightly improved the thermal stability of the PVDF-PW@PPy composite membrane. Besides, there was no obvious thermal decomposition or weight loss within 100 °C, which means that the prepared PVDF-PW@PPy can keep stable performance in the working temperature range.

Conductivity determines both Joule heating capacity and EMI shielding efficacy. As a typical conductive polymer, PPy forms continuous conductive pathways on the surface of PVDF-PW fibre membranes, and the polymerization time significantly influences the formation of these pathways. In order to ensure superior output performance, the conductivity of the composite films under different polymerisation times was tested. It can be seen that the conductivity of the PVDF-PW@PPy composite films ranged from 0.74 to 1.35 S/cm. With increasing polymerization time, the conductivity initially increased and subsequently decreased, reaching a maximum value after 4 h of polymerization (Figure 2a). Hence, the subsequent discussion will only focus on the PVDF-PW@PPy composite film with polymerisation time of 4 h based on the results of microstructural analysis, thermal energy storage capacity, and electrical conductivity testing.

We then investigated the resistance characteristics of the composite film, which is crucial for Joule heating

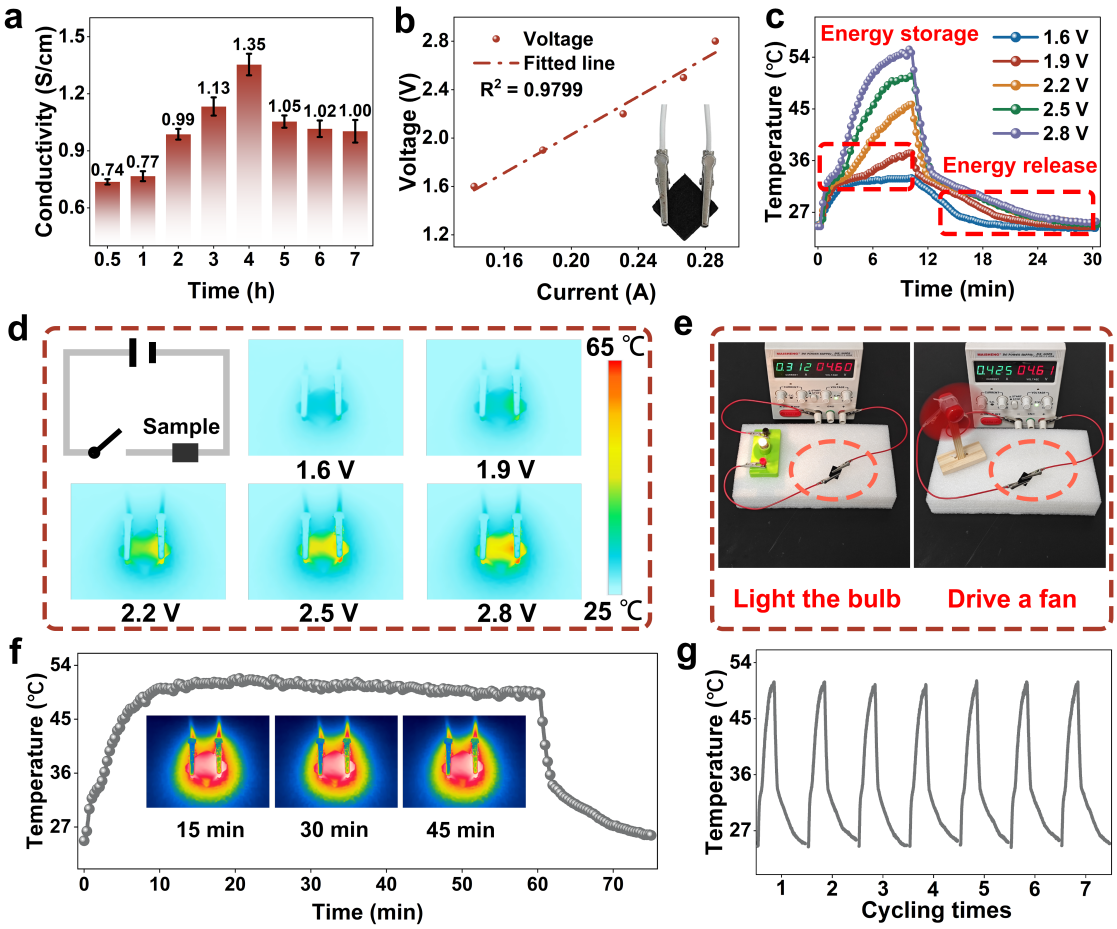

Figure 2 Electro-to-thermal conversion testing of PVDF-PW@PPy composite films. (a) Electrical conductivity of the composite film at different polymerisation times. (b) Voltage-current (*V-I*) curve of the composite film. (c) Temperature of the composite film at different test voltages. (d) Principle of the electro-to-thermal conversion test and a representative infrared thermal image captured at 10 min after applying a voltage of 2.5 V. (e) Images of composite film illuminating a bulb or driving a small fan within a closed circuit. (f) Temperature curve of the composite film during long-time testing. (g) Temperature curve of the composite film during seven continuous tests at 2.5 V.

properties. The voltage at the two ends of PVDF-PW@PPy composite film was proportional to the current passing through ($R^2 = 0.98$) under testing voltage of 1.6–2.8 V, demonstrating excellent ohmic characteristics (Figure 2b). Furthermore, when incorporated into an electrical circuit, the composite film can illuminate a bulb or drive a fan, confirming its excellent conductivity and the potential for electrical-to-thermal conversion (Figure 2e). Based on this characteristic, the surface temperature of the composite film at different voltages was recorded. The relevant test circuit and some infrared thermal imaging diagrams are shown in Figure 2d. When the circuit was connected, the surface temperature rose rapidly as the electrical energy provided by the power source could be promptly converted into the thermal energy of PVDF-PW@PPy, while the temperature dropped sharply when the circuit was disconnected (Figure 2c). It can be observed that once the power switch was turned on, the temperature can rise rapidly within a few seconds, demonstrating excellent temperature response capability. At different test voltages, the recorded maximum temperatures within 10 min were 33.1, 37.4, 45.8, 50.7, and 55.2 °C, respectively. It shows that the intended temperature can be adjusted through appropriate input voltage and charging time, making the PVDF-PW@PPy composite

film a potential alternative for specific thermal therapy requirements [41]. Notably, distinct phase change plateaus were observed during both heating and cooling processes, corresponding to the solid-liquid and liquid-solid transitions of the PW, respectively. In addition, the composite film also features a stable electrical-to-thermal conversion capability, whose temperatures remained largely unchanged throughout a prolonged one-hour test (Figure 2f). Even after seven consecutive operational cycles at 2.5 V, it still achieves stable output performance, demonstrating excellent cycling reliability (Figure 2g).

The composite film also exhibits impressive solar-to-thermal conversion capability. Benefited from the strong light-trapping ability of PPy, the absorbance of PVDF-PW@PPy was increased from 7.46% to 95.47% within the solar spectrum (AM 1.5) after PPy polymerisation (Figure 3a). To evaluate the actual solar-to-thermal conversion performance of the PVDF-PW@PPy, a test apparatus was constructed (Figure 3b). When the simulated Xenon lamp was turned on, the temperature of the composite film rose sharply due to the light energy was converted into the thermal energy of PVDF-PW@PPy, and the temperature dropped rapidly when the Xenon lamp was turned off (Figure 3c). Figure 3d shows a partial infrared (IR) thermal image of the sample under 1.0 sun (1.0 kW/m^2) radiation. The maximum temperatures of the composite film under 10 min illumination at 0.6–1.0 sun were 39.1, 42.5, 44.7, 47.5, and 50.2 °C, respectively. During the heating process, a distinct phase change plateau was also observed in the temperature range of 32–40 °C, indicating that the PW inside PVDF-PW@PPy can effectively store the solar energy in the form of latent heat. During the cooling process, the cooling rate significantly decreases below 30 °C, which is attributed to the release of heat stored within PW. In contrast, the maximum temperature of PVDF-PW reached only 28.9 °C under the same light intensity and exposure time. Even when the light intensity increased to 2.0 sun, the elevated temperature was still far behind that of the PVDF-PW@PPy composite film (Figure 3e and f). It can be attributed to the PVDF-HFP coating on the surface of PVDF-PW, which exhibits strong reflectivity and significantly impedes the effective absorption and conversion of solar energy. When PPy nanoparticles were loaded, the light-absorbing capacity of PVDF-PW composite film was greatly enhanced. The solar-to-thermal conversion efficiency (η) of the composite can be obtained using the following formula [6,42,43]:

$$\eta = \frac{m \times \Delta H_{\mathrm{m}}}{P \times S \times (t_2 - t_1)}.$$

The specific parameters are shown in Table S1. It could be seen that the η was increased with light intensity since the heat provided by the solar energy could be transformed into the thermal energy of PVDF-PW@PPy composite film in time. After 10 min of irradiation at 0.6 sun light intensity, the energy absorbed by the composite film was insufficient to support the complete phase transition of PW within the film from solid to liquid state. A completed phase transition process can be achieved once the light intensity exceeds 0.6 sun. Hence, the value of η was increased from 62.02% to 93.95% when the light intensity rose from 0.7 sun to 1.0 sun (Figure 3g). Even during ten continuous tests, the temperature rise curves and peak temperatures remained largely the same, confirming the stable solar-to-thermal conversion capability of PVDF-PW@PPy (Figure 3h).

The solar-to-thermal conversion mechanism of PVDF-PW@PPy can be explained by Figure 3i. First, the PVDF-PW membrane was composed of numerous interlaced fibres. The specific surface area of the prepared PVDF-PW@PPy composite film was greatly enhanced after polymerisation of a number of nanoscale PPy molecules. Moreover, the composite film also exhibits numerous pore structures at micro- and nanoscale levels. These hierarchical porous structures can effectively enhance the interaction between light and PVDF-

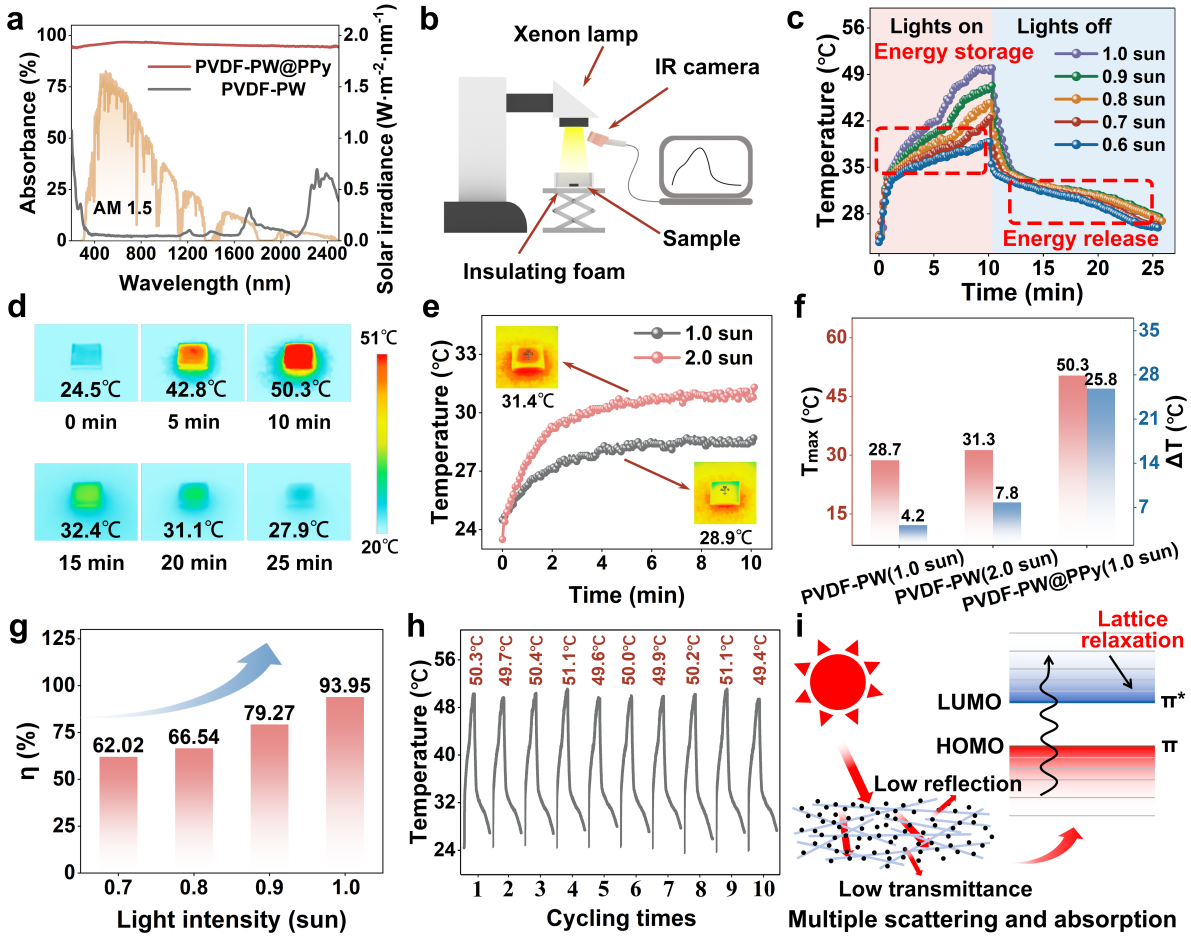

Figure 3 Solar-to-thermal conversion testing of PVDF-PW@PPy. (a) Absorbance of the composite film. (b) Schematic diagram of the solar-to-thermal conversion testing device. (c) Temperature curves of PVDF-PW@PPy under different light intensities. (d) Partial infrared thermal imaging during testing. (e) Temperature curves under 1.0 and 2.0 sun light intensities. (f) Maximum temperature and temperature difference under different test conditions. (g) Solar-to-thermal conversion efficiency under different light intensities. (h) Temperature curves of the composite film under ten continuous photothermal conversion tests. (i) Solar-to-thermal conversion mechanism.

PW@PPy through light capture effects and extend the light path [44,45]. As a result, most of the light can be effectively absorbed, while only a small portion is dissipated through reflection and transmission. In addition, the pyrrole ring of PPy features a substantial number of highly conjugated π electron systems, which helps to reduce the energy difference between the highest occupied molecular orbital (HOMO) and the lowest unoccupied molecular orbital (LUMO) [46]. The conjugated double bonds inside PPy are more likely to undergo a transition from π to π* under solar radiation [47,48]. Once the PVDF-PW@PPy composite film was exposed to the energy that could trigger electron transitions, the absorbed light would excite electrons from the ground state to a higher energy orbit. These excited electrons would then return to the ground state through intense lattice relaxation and convert solar energy into heat energy [49]. Hence, the prepared PVDF-PW@PPy composite film has an excellent solar-to-thermal conversion ability, which is beneficial for efficient solar energy capture and utilisation.

In addition to active thermal management capabilities, EMI shielding presents another critical challenge for both human health and electronic devices [50]. In order to evaluate the EMI shielding capability of the

PVDF-PW@PPy, the values of EMI SE were tested (Figure 4a). Pure PVDF-PW film exhibits negligible SE. In contrast, the PVDF-PW@PPy composite membrane achieves an average SE of 20.43 dB at a density of 0.26 g/cm^3, satisfying commercial requirements of 20 dB [51]. It indicates that the aggregated PPy has a significant influence on the EMI shielding performance. Additionally, the PVDF-PW@PPy composite film can be folded into multi-layer structures via a simple origami technique owing to the superior mechanical flexibility. The SE of the composite film reached 23.29 and 29.71 dB after one-time and two-time folding, respectively. According to Schelkunoff's theory, the total SE (SE_T) can be divided into the absorption efficiency (SE_A) and the reflection efficiency (SE_R) when SE_T exceeds 15 dB. To further analyse the EMI shielding properties of PVDF-PW@PPy, SE_A and SE_R were calculated. The values of SE_R remained nearly unchanged across different folding counts (4.93–7.15 dB). In contrast, the SE_A increased from 15.25 to 24.78 dB when the folding number was two (Figure 4b). Moreover, the ratio of SE_A to SE_R in different layer membranes ranged from 2.3 to 5.0 (Figure 4c).

The EMI shielding mechanism of PVDF-PW@PPy is illustrated in Figure 4d. The aggregated PPy forms a conductive layer along with the PVDF-PW coaxial electrospun fibres. This results in the incident EMWs being partially reflected back into the environment upon encountering the composite film surface due to the severe impedance mismatch between the composite film and the surrounding air [52]. The residual EMWs penetrate into the porous PVDF-PW@PPy, where a portion interacts with the deposited PPy and attenuates to generate ohmic losses [53]. According to the Maxwell-Wagner-Sillars interface polarisation principle, the highly conductive network structure of PPy provides an ample supply of mobile charge carriers at the membrane surface. This enhances the polarisation effect at the interface between the fibre and air, thereby promoting the dissipation of EMWs [54]. Moreover, the rough fibre structure effectively extends the propagation path of EMWs, facilitating their gradual attenuation through multiple reflection and scattering processes within the interstitial spaces of the composite membrane [19]. Consequently, the majority of them were ultimately absorbed and converted into thermal energy, with only a small fraction transmitting through the composite membrane. Hence, the enhancement of SE_T through folding can be primarily attributed to a significant increase in SE_A. The origami-inspired folding process creates a multi-layer structure with additional air-material interfaces and more intricate internal conductive networks. When incident EMWs penetrate this layered assembly, they undergo repeated reflection and scattering between the internal interfaces and the conductive PPy layers. This process effectively prolongs the propagation path of the EMWs within the material, allowing for more efficient energy dissipation through ohmic and polarization losses. Consequently, the SE_A rises markedly, as observed in Figure 4b, while the SE_R remains relatively constant. This absorption-dominant shielding mechanism is highly desirable, as it minimizes secondary electromagnetic pollution [55,56].

We also verified the actual EMI shielding performance of PVDF-PW@PPy through a simple device, as shown in Figure 4e. When the switch of the device was turned on, a wireless light-emitting diode (LED) positioned near the Tesla coil could be illuminated due to the presence of the electromagnetic field. When the PVDF-PW membrane was inserted between the LED and the Tesla coil, the brightness of the bulb remained unaffected. By contrast, the bulb was extinguished when the PVDF-PW@PPy composite membrane was inserted, as the electromagnetic signals generated by the Tesla coil were isolated or disrupted. Once the composite film was removed, the LED could return to its original brightness rapidly. Hence, it further demonstrates that the prepared PVDF-PW@PPy composite film exhibits excellent EMI shielding perfor-

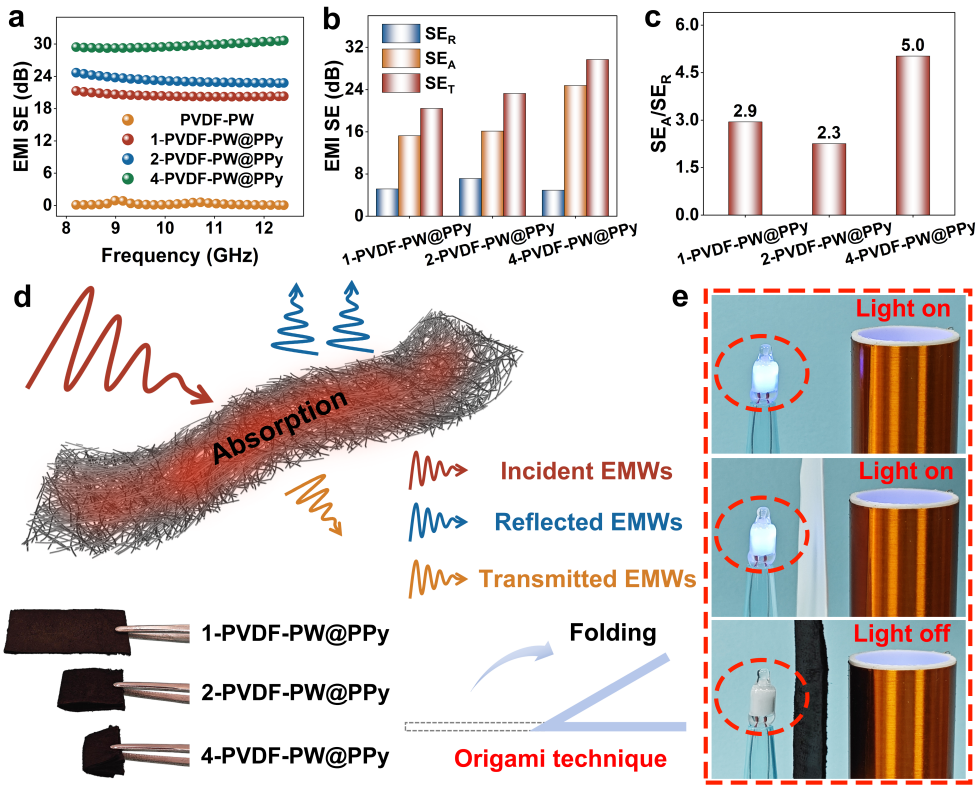

Figure 4 EMI shielding performance testing of PVDF-PW@PPy. (a) EMI values of the composite film at different frequencies. (b) SE_R, SE_A, and SE_T values of the composite film. (c) Ratio of SE_A to SE_R. (d) EMI shielding mechanism. (e) Practical application of EMI shielding.

mance.

In addition, the PVDF-PW@PPy composite film also features a favourable thermal reliability. We subjected it to 100 thermal cycles between room temperature and 70 °C and compared the performance before and after testing. The FT-IR and optical absorption properties of the composite film remained basically unchanged (Figure S14), while the absorbance decreased slightly by 2.25% (Figure S15). All the DSC curves, enthalpy values, and phase change temperatures of the samples were nearly consistent before and after testing, indicating that the PVDF-PW@PPy composite film can maintain stable thermal properties during multiple heating and cooling cycles (Figure S16). The stable phase change energy storage capability and thermal reliability ensure a more comprehensive role for PVDF-PW@PPy in the field of thermal management.

CONCLUSIONS

In summary, an advanced composite film integrating passive and active thermal management capabilities with EMI shielding performance was presented in this study based on interfacial engineering strategies. The composite film obtained via coaxial electrospinning exhibits excellent flexibility and phase change energy storage capacity (82.84 J/g). Subsequently, the *in situ* polymerised PPy nanoparticles formed continuous

electronic conduction pathways along the fibres, endowing the composite membrane with active thermal management capabilities, including both Joule heating and solar-to-thermal conversion functions. Such a membrane achieves a solar-to-thermal conversion efficiency of 93.95% under 1.0 sun irradiation. Moreover, it exhibits satisfactory EMI shielding performance, and the EMI SE can be enhanced to 29.71 dB through a simple origami technique. In summary, the prepared PVDF-PW@PPy exhibits broad application in both thermal management and EMI shielding areas, providing significant insights for the construction of lightweight, flexible and sustainable multifunctional wearable textiles.

METHODS

Detailed materials and methods are available in the Supplementary information online.

Data availability

The original data are available from corresponding authors upon reasonable request.

Funding

This work was supported by the National Natural Science Foundation of China (52473033).

Author contributions

X.H. and X.L. designed the experiments. R.W., B.Q. and M.H. carried out the experiments. R.W. and X.H. analyzed the data and wrote the manuscript. R.W., X.H. and X.L. discussed the results and commented on the manuscript.

Conflict of interest

The authors declare no conflict of interest.

Supplementary information

The supporting information is available online at https://doi.org/10.1360/nso/20250063. The supporting materials are published as submitted, without typesetting or editing. The responsibility for scientific accuracy and content remains entirely with the authors.

References

1 Liu L, Yuan D, Hu X, *et al.* Wind-proof and moisture permeability aerogel-functionalized textile as all-seasonal passive thermal regulators. *Adv Funct Mater* 2024; **34**: 2411551.

2 Yang P, Ju Y, He J, *et al.* Advanced Janus membrane with directional sweat transport and integrated passive cooling for personal thermal and moisture management. *Adv Fiber Mater* 2024; **6**: 1765–1776.

3 Liu H, Xiao Y, Shen Y, *et al.* Self-adaptive rapid thermal conductive fabrics based on hygroscopic shrinkage response for personal cooling and drying. *ACS Appl Mater Interfaces* 2024; **16**: 7917–7926.

4 Dang C, Wang Z, Hughes-Riley T, *et al.* Fibres—threads of intelligence—enable a new generation of wearable systems. *Chem Soc Rev* 2024; **53**: 8790–8846.

5 Niu P, Mao H, Lim KH, *et al.* Nanocellulose-based hollow fibers for advanced water and moisture management. *ACS Nano* 2023; **17**: 14686–14694.

6 Niu Z, Yuan W. Smart nanocomposite nonwoven wearable fabrics embedding phase change materials for highly efficient energy conversion-storage and use as a stretchable conductor. *ACS Appl Mater Interfaces* 2021; **13**: 4508–4518.

7 Gu B, Li G, Zhang Q, *et al.* A novel method for increasing phase-change microcapsules in nanofiber textile through electrospinning. *Adv Funct Mater* 2024; **35**: 2412089.

8 Li X, Sheng X, Fang Y, *et al.* Wearable Janus-type film with integrated all-season active/passive thermal management, thermal camouflage, and ultra-high electromagnetic shielding efficiency tunable by origami process. *Adv Funct Mater* 2023; **33**: 2212776.

9 Xu F, Zhang T, Xu Z, *et al.* Solid-solid phase change fibers with enhanced energy storage density for temperature management. *J Energy Storage* 2024; **79**: 110190.

10 Wang Y, Hu J, Jia Y, *et al.* Nano-structured multicores-sheath thermoregulation textile with room temperature phase change point via coaxial electrospinning. *J Energy Storage* 2024; **100**: 113639.

11 Lin Y, Jia Y, Alva G, *et al.* Review on thermal conductivity enhancement, thermal properties and applications of phase change materials in thermal energy storage. *Renew Sustain Energy Rev* 2018; **82**: 2730–2742.

12 Guo D, Mu C, Liu Q, *et al.* Aramid nanofiber/polypyrrole composite films for broadband EMI shielding, wearable electronics, Joule heating, and photothermal conversion. *ACS Appl Nano Mater* 2023; **6**: 15108–15118.

13 Yang D, Zhou B, Han G, *et al.* Flexible transparent polypyrrole-decorated MXene-based film with excellent photothermal energy conversion performance. *ACS Appl Mater Interfaces* 2021; **13**: 8909–8918.

14 Gong X, Xiang L, Qi X, *et al.* Improved polarization loss and impedance matching induced by carbon paper-based magnetic heterostructured composites for lightweight and strong microwave absorption. *Adv Compos Hybrid Mater* 2024; **7**: 216.

15 Jiang H, Sun H, Zhang S, *et al.* Lightweight and high-performance carbon nanotube fabrics for electromagnetic interference shielding. *Sci China Mater* 2025; **68**: 2071–2078.

16 Jia T, Hao Y, Qi X, *et al.* Interface engineering and impedance matching strategy to develop core@shell urchin-like NiO/Ni@carbon nanotubes nanocomposites for microwave absorption. *J Mater Sci Tech* 2024; **176**: 1–12.

17 Wang ZL, Wang M, Li LX, *et al.* Permeation behavior of low-melting-point Sn–Bi alloy in the fiber channel of pine wood. *Mater Des* 2020; **196**: 109068.

18 Kim J, Hong M, Lee D, *et al.* Mechanically robust phase-change multiscale-architected metastructures integrating asymmetric MXene/T-CNF aerogel for thermal energy storage and electromagnetic interference shielding. *Adv Funct Mater* 2025; e14180.

19 Cao Y, Zhao Z, Zeng X, *et al.* High-performance polyimide/polypyrrole-CNTs@PEG composites for integrated thermal management and enhanced electromagnetic wave absorption. *Adv Compos Hybrid Mater* 2025; **8**: 104.

20 Wang H, Xiao J, Qi X, *et al.* Microstructural optimization and non-metallic doping strategy to develop mesoporous N-doped carbon hollow nanospheres for strong and broadband microwave absorption. *J Mater Sci Tech* 2026; **247**: 55–63.

21 Chu G, Nie Z, Peng Y, *et al.* Spin-coating ANF based multilayer symmetric composite films for enhanced electromagnetic interference shielding and thermal management. *J Colloid Interface Sci* 2025; **679**: 521–530.

22 Zhang X, Li J, Gao Q, *et al.* Nerve-fiber-inspired construction of 3D graphene "Tracks" supported by wood fibers for multifunctional biocomposite with metal-level thermal conductivity. *Adv Funct Mater* 2023; **33**: 2213274.

23 Zhao Y, Chen H, Qiao S, *et al.* Hierarchically porous polyimide/graphene aerogels with superior compressibility and electromagnetic interference shielding performance. *J Mater Chem A* 2025; **13**: 22613–22620.

24 Singh AK, Shishkin A, Koppel T, *et al.* A review of porous lightweight composite materials for electromagnetic interference shielding. *Compos Part B-Eng* 2018; **149**: 188–197.

25 Du J, Li T, Li J, *et al.* Design of flexible MXene/graphene-based fiber fabrics for broadband electromagnetic wave absorption. *Adv Fiber Mater* 2025; **7**: 811–826.

26 Iqbal A, Sambyal P, Koo CM. 2D MXenes for electromagnetic shielding: A review. *Adv Funct Mater* 2020; **30**: 2000883.

27 Gao C, Li Y, Lan L, *et al.* Bioinspired asymmetric polypyrrole membranes with enhanced photothermal conversion for highly efficient solar evaporation. *Adv Sci* 2023; **11**: 2306833.

28 Wu H, Chen R, Shao Y, *et al.* Novel flexible phase change materials with mussel-inspired modification of melamine foam for simultaneous light-actuated shape memory and light-to-thermal energy storage capability. *ACS Sustain Chem Eng* 2019; **7**: 13532–13542.

29 Li Y, Diao X, Li P, *et al.* Advanced multifunctional Co/N co-doped carbon foam-based phase change materials for wearable thermal management. *Chem Eng J* 2024; **485**: 149858.

30 Wu H, Li S, Shao Y, *et al.* Melamine foam/reduced graphene oxide supported form-stable phase change materials with simultaneous shape memory property and light-to-thermal energy storage capability. *Chem Eng J* 2020; **379**: 122373.

31 Chen Z, Li J, Zhou J, *et al.* Photothermal Janus PPy-SiO_2@PAN/F-SiO_2@PVDF-HFP membrane for high-efficient, low energy and stable desalination through solar membrane distillation. *Chem Eng J* 2023; **451**: 138473.

32 Liu JZ, Jiang W, Zhuo S, *et al.* Large-area radiation-modulated thermoelectric fabrics for high-performance thermal management and electricity generation. *Sci Adv* 2025; **11**: eadr2158.

33 Wang T, Yang Y, Wei R, *et al.* High-performance and anti-leakage polypyrrole-modified wood-based composite phase change material with superior photothermal conversion capability. *J Energy Storage* 2025; **113**: 115696.

34 Guo T, Li X, Zhou H, *et al.* Effect of large-sized hydrophilic polypyrrole on electrochemical properties of MXene films. *J Power Sources* 2024; **593**: 233978.

35 Dai H, Yuan J, Kong X, *et al.* Shape-memory phase change material enhanced by MWCNT for solar photothermal conversion. *Sol Energy Mater Sol Cells* 2024; **269**: 112756.

36 Lei D, Hu N, Wu L, *et al.* Improvement of the piezoelectricity of PVDF-HFP by $CoFe_2O_4$ nanoparticles. *Nano Mater Sci* 2024; **6**: 201–210.

37 Li Y, Shan M, Peng J, *et al.* A highly stretchable and conductive continuous composite filament with buckled polypyrrole coating for stretchy electronic textiles. *Appl Surf Sci* 2023; **610**: 155515.

38 Gan W, Chen C, Giroux M, *et al.* Conductive wood for high-performance structural electromagnetic interference shielding. *Chem Mater* 2020; **32**: 5280–5289.

39 Kong L, Li YJ, Kong X, *et al.* A novel flexible and fluoride-free superhydrophobic thermal energy storage coating for photothermal energy conversion. *Compos Part B-Eng* 2022; **232**: 109588.

40 Hu Y, Wang T, Cheng C, *et al.* Skeleton of PVDF-HFP/PEO for high-performance lithium-sulfur battery cathode. *J Energy Storage* 2024; **100**: 113631.

41 Wu Y, Dong L, Tang S, *et al.* An innovative azobenzene-based photothermal fabric with excellent heat release performance for wearable thermal management device. *Small* 2024; **20**: 2404310.

42 Hou M, Chen H, Li S, *et al.* A Tri-mode photothermal, phase-change, and radiative-cooling film for all-day thermoelectric generation. *Adv Mater* 2025; **37**: 2505601.

43 Yang J, Tang LS, Bao RY, *et al.* Largely enhanced thermal conductivity of poly (ethylene glycol)/boron nitride composite phase change materials for solar-thermal-electric energy conversion and storage with very low content of graphene nanoplatelets. *Chem Eng J* 2017; **315**: 481–490.

44 Chai Z, Fang M, Min X. Composite phase-change materials for photo-thermal conversion and energy storage: A review. *Nano Energy* 2024; **124**: 109437.

45 Zhou M, Zhang L, Zhong L, *et al.* Robust photothermal icephobic surface with mechanical durability of multi-bioinspired structures. *Adv Mater* 2023; **36**: 2305322.

46 Hou L, Li S, Qi Y, *et al.* Advancing efficiency in solar-driven interfacial evaporation: Strategies and applications. *ACS Nano* 2025; **19**: 9636–9683.

47 Li S, Zhang N, Chen H, *et al.* Encapsulating phase change materials into melamine formaldehyde sponge assembled with polypyrrole modified halloysite nanotube for effective solar-thermal energy storage and solar-thermal-electric conversion. *J Colloid Interface Sci* 2025; **682**: 423–435.

48 He J, Liu F, Xiao C, *et al.* Fe_3O_4/PPy-coated superhydrophilic polymer porous foam: A double layered photothermal

material with a synergistic light-to-thermal conversion effect toward desalination. *Langmuir* 2021; **37**: 12397–12408.

49 Liu P, Huang M, Chen X, *et al.* Polypyrrole-boosted photothermal energy storage in MOF-based phase change materials. *Interdiscip Mater* 2023; **2**: 423–433.

50 Liang Q, He M, Zhan B, *et al.* Yolk-shell CoNi@N-doped carbon-CoNi@CNTs for enhanced microwave absorption, photothermal, anti-corrosion, and antimicrobial properties. *Nano-Micro Lett* 2025; **17**: 167.

51 Zhang Y, Kong J, Gu J. New generation electromagnetic materials: Harvesting instead of dissipation solo. *Sci Bull* 2022; **67**: 1413–1415.

52 Zhou M, Wang J, Zhao Y, *et al.* Hierarchically porous wood-derived carbon scaffold embedded phase change materials for integrated thermal energy management, electromagnetic interference shielding and multifunctional application. *Carbon* 2021; **183**: 515–524.

53 Zhang X, Yang Y, Yang G, *et al.* Robust PI composites with high-connected AgNPs for multifunctional electromagnetic interference shielding in harsh environment. *Compos Part B-Eng* 2025; **305**: 112735.

54 Lee S, Nguyen NK, Kim M, *et al.* Conductivity-controlled polyvinylidene fluoride nanofiber stack for absorption-dominant electromagnetic interference shielding materials. *ACS Appl Mater Interfaces* 2023; **15**: 33180–33189.

55 Chen Y, Meng Y, Zhang J, *et al.* Leakage proof, flame-retardant, and electromagnetic shield wood morphology genetic composite phase change materials for solar thermal energy harvesting. *Nano-Micro Lett* 2024; **16**: 196.

56 Xiao J, Zhan B, He M, *et al.* Mechanically robust and thermal insulating nanofiber elastomer for hydrophobic, corrosion-resistant, and flexible multifunctional electromagnetic wave absorbers. *Adv Funct Mater* 2025; **35**: 2419266.